Journal of Materials Chemistry B

ROYAL SOCIETY OF CHEMISTRY

PAPER

Published on 21 July 2026

Cite this: DOI: 10.1039/d6tb00750c

Tailoring the morphology and crystallinity of MoS_2 for bacterial inhibition of Gram-negative and Gram-positive bacteria

Joseph Monahan,[a] Shauna O'Shea-Boland,[b] Fiona Walsh[b] and Carmel B. Breslin *[a]

Received 1st April 2026,
Accepted 20th July 2026

DOI: 10.1039/d6tb00750c

rsc.li/materials-b

Antimicrobial resistance causes millions of infections and deaths each year, necessitating new approaches to minimise these effects. Here, we present a direct comparison of crystalline, MoS_2 nanosheets (MNS) and amorphous MoS_2 nanoflowers (MNF) against *Escherichia coli* MG1655 (Gram-negative bacteria) and *Staphylococcus aureus* RN4220 (Gram-positive bacteria). The crystalline MNS sheets of different sizes were obtained using exfoliation of bulk MoS_2, while the amorphous MNF was formed using hydrothermal synthesis. Using XPS, the MNF was found to contain MoO_3 in addition to MoS_2, while the MNS had little or no impurities. The MNS exhibited a Zeta potential of −29.4 mV, while MNF showed a lower potential of −23.5 mV, indicating greater dispersibility of the MNS in aqueous-based biological media. Utilising a combination of Ellman's, nitroblue tetrazolium, and terephthalic acid assays, the crystalline MNS was observed to favour superoxide-linked oxidative stress, which proved particularly effective against *Escherichia coli*. Conversely, the amorphous MNF produced hydroxyl radicals that facilitated early GSH oxidation, thereby favouring inhibition of *Staphylococcus aureus*. In both cases, there was no evidence of membrane cell damage.

Introduction

The World Health Organisation (WHO) has classified antimicrobial resistance (AMR) as one of the most significant challenges to human health. In 2019, it was estimated that bacterial AMR was directly responsible for 1.27 million deaths globally, having contributed to 4.95 million deaths.[1] The rise of this resistance is driven by a number of factors, including antimicrobial overuse in human medicine and agriculture, and vaccination reluctance.[2] Not surprisingly, the pharmaceutical industry faces tremendous pressure to continually develop new antibacterial treatments to combat emerging, resistant strains. Attention has now turned to alternative methods to prevent the development, accumulation and spread of AMR.

An essential strategy for tackling AMR is to limit the spread of infection by targeting contaminated surfaces, which are now recognised as key vectors for microbial transmission. Contaminated surfaces are recognised as an important route for the transmission of microorganisms in a variety of environments, including hospitals, food-processing plants and public areas. Many clinically relevant bacteria, including *E. coli* and *S. aureus*, have been shown to persist on dry surfaces for prolonged periods.[3] These surfaces can then act as reservoirs for bacterial transmission. Current cleaning and disinfection methods can reduce surface contamination, however, recolonisation can occur rapidly.[4] This highlights the need for materials which can provide sustained antibacterial protection. Such intrinsically antibacterial materials can be integrated into coatings, polymeric substrates and textiles to deliver continuous protection and lower the risk of surface colonisation and infection.

In this regard, nanomaterials have become a focus as unconventional antimicrobial agents due to their distinctive physical and chemical properties. These nanomaterials offer a different perspective to their macroscopic predecessors due to their increased surface area and their variable shape and morphology. A wide variety of nanomaterials have been explored as potential antibacterial agents, including carbon-based nanomaterials,[5] metal nanoparticles,[6] and metal oxides and sulfides.[7] One nanomaterial family of particular interest are the two-dimensional transition metal dichalcogenides (2D-TMDs). These are a family of van der Waals layered materials which have a wide variety of applications in electrochemistry,[8] phototherapy and biomedicine.[9] Molybdenum disulfide (MoS_2) is the most prominent of this family. MoS_2 is commonly seen as

[a] Department of Chemistry and Kathleen Lonsdale Human Health Institute, Maynooth University, Maynooth, Co. Kildare, Ireland. E-mail: Carmel.Breslin@mu.ie
[b] Department of Biology and Kathleen Lonsdale Human Health Institute, Maynooth University, Maynooth, Co. Kildare, Ireland

a bulk material which is then exfoliated, through numerous methods, to yield single/few-layered nanosheets.[10] However, MoS_2 can be synthesised by other methods to yield other morphologies. Hydrothermal synthesis accompanied by various surfactants has been reported to yield a variety of 2D-TMD morphologies, including flowers,[11] spheres and rods.[12]

The performance of MoS_2 in its various applications is strongly influenced by its size, structure and morphology. MoS_2 nanosheets and similarly structured materials, such as graphene oxide, have been reported to exert a physical, 'knife-like' action on bacterial cells.[13] This physical action has been reported to confer MoS_2 nanosheets with superior antibacterial activity compared to that of bulk MoS_2.[14] Both membrane damage due to the knife-like action, as evidenced by scanning electron microscopy,[15] and a wrapping effect have been proposed to account for the antibacterial mechanism.[16] With wrapping, the sheets encase the bacterial cells, depriving them of the nutrients necessary for growth and proliferation. Larger sheets have shown more effective wrapping. A similar wrapping effect has been reported for graphene.[17] In addition, MoS_2 acts as a semiconductor, generating reactive oxygen species (ROS), particularly the superoxide anion ($O_2^{\bullet -}$), and ROS-independent oxidative stress by glutathione oxidation. MoS_2 nanoflowers have similarly been reported to generate ROS, causing ROS-independent oxidative stress[18] in bacterial species, with higher ROS generation under visible-light irradiation.[19]

In this work, the influence of this morphological difference on the antibacterial inhibition of Gram-negative bacteria (GNB) and Gram-positive bacteria (GPB) was studied. GNB have been reported to be more susceptible to physical membrane damage due to their thinner peptidoglycan layer, which is approximately 10-fold thinner than that of GPB.[17] GNB have also been shown to be more susceptible to oxidative stress (ROS-dependent and ROS-independent) and are particularly susceptible to oxidative stress during their exponential growth phase,[18] making oxidative stress important for the inhibition of bacterial growth.

While previous research has explored the antibacterial properties of MoS_2 nanosheets and nanoflowers/flowers individually, no studies to date have systematically compared these morphologies against both GNB and GPB to determine the role of morphology in inhibition activities. Here, crystalline MoS_2 nanosheets and amorphous MoS_2 nanoflowers are directly contrasted to establish how morphology, crystallinity, surface chemistry, and colloidal stability govern strain-dependent antibacterial selectivity. *Escherichia coli* (*E. coli*) MG1655 (GNB model) and *Staphylococcus aureus* (*S. a ureus*) RN4220 (GPB model) were used to determine the effect of the nanostructure morphology on bacterial inhibition. The MoS_2 nanosheets (MNS) had more potent inhibition against *E. coli*. In contrast, the MoS_2 nanoflowers (MNF) more effectively targeted *S. aureus*. To understand the inhibition mechanism, ROS production was investigated using a nitroblue tetrazolium (NBT) assay to detect superoxide anions, a terephthalic acid (TA) assay to detect hydroxyl radicals, and an Ellman's assay was employed to assess *in vitro* glutathione oxidation. These findings contribute to the structure–activity relationships of TMDs as antibacterial materials and highlight their potential for tailored applications in combating antimicrobial resistance.

Experimental

Materials and methods

All chemicals used were of analytical reagent grade and did not require further purification before use. These chemicals included MoS_2 (<2 μm), sodium molybdate dihydrate, thiourea, D-(+)-glucose, nitro blue tetrazolium (NBT), dimethyl sulfoxide (DMSO), 5,5′-dithiobis-(2-nitrobenzoic acid) (DNTB), propidium iodide solution and glutathione, and these were all purchased from Merck.

Exfoliation of the nanosheets was carried out using a probe sonicator, VCX500 (500 W, and 20 kHz). The temperature was maintained at 25 °C. Centrifugation was performed using a ThermoFisher Sorvall ST 8. To give nanosheets of different sizes, the exfoliated bulk MoS_2 was centrifuged, and the supernatant was collected. This was repeated several times to obtain supernatants containing MoS_2 sheets of different sizes. Incubation and absorbance measurements at an optical density (OD) of 600 nm were carried out using the BMG Clariostar multimode microplate reader.

Preparation of MoS_2 nanosheets (MNS) and MoS_2 nanoflowers (MNF)

Commercial molybdenum disulfide powders (30 mL, 5 mg mL^{-1}) were exfoliated by liquid-phase exfoliation and refluxing in an ethanol : water (50 : 50) solvent system. A sonication probe was used to exfoliate the bulk material into single/few-layered sheets. Sheets were exfoliated for 15 min with a pulse-on/off ratio (20 s on and 10 s off). Then 0.75 g D-(+)-glucose and 0.1 g NaOH were added to the 30 mL solution, and the mixture was stirred for 10 min. The resulting dispersion was refluxed in an oil bath at 85 °C for 5 h. The refluxed sheets were then washed with deionised water (dH_2O) followed by ethanol and dried at 60 °C for 12 h. Refluxing for 1, 3, and 10 h was also performed to determine the optimum reflux time for exfoliation. The optimal bacterial efficiency was achieved with the 5 h reflux period. MoS_2 nanoflowers were prepared as reported.[20] In short, 0.77 g of $Na_2MoO_4{\cdot}2H_2O$, 1.22 g of $CS(NH_2)_2$ and 1 g of D-(+)-glucose were solubilised in 30 mL of dH_2O. The solution was then transferred to a 100 mL Teflon-lined autoclave and placed into an oven at 180 °C for 6 h. The system was allowed to cool. The resulting product was thoroughly washed with dH_2O and ethanol and dried at 60 °C for 12 h.

Characterisation studies

The crystallinity and phases of the MoS_2 nanostructures were measured using powder X-ray diffraction (P-XRD) (PANalytical, X'Pert-PRO MPD system). The chemical state of the elements on the sample surface was determined using X-ray photoelectron spectroscopy (XPS) (XPS Kratos AXIS ULTRA spectrometer). The absorbance of the samples was measured with UV-visible spectroscopy (Cary 50 spectrometer). The surface morphology

of the nanostructures was investigated using scanning electron microscopy (SEM) (Thermo Fisher Phenom ProX Gen 4 desktop SEM), and transmission electron microscopy (TEM) with FEI Titan Themis Cubed G2 60–300 kV double-aberration-corrected monochromated instrument. To assess the particle size distribution and stability after dispersion, Zeta potential and dynamic light scattering tests were carried out using a liquid zeta particle size/potential analyser (DLS) (Malvern Zetasizer Pro).

Cell preparation for biological studies

E. coli MG1655 and *S. aureus* RN4220 were used in this work. For each species, a single bacterial colony was inoculated overnight in 3 mL of LB Broth at 37 °C, shaking at 225 rpm. The bacterial culture was diluted 1/100 (30 μL of bacterial solution in 2970 μL LB Broth), and this was grown for 1 h at 37 °C, shaking. The bacteria were then grown to an OD_{600} = 0.2 (1.6×10^8 CFU). Serial dilutions were then performed to yield a final bacterial concentration of 1.6×10^4 CFU.

Assay for antibacterial activity of MNS and MNF

Bacterial inhibition by the MNF and MNS was determined by measuring optical density at 600 nm. The ability of these materials to inhibit bacterial growth was investigated against both *E. Coli* and *S. aureus*. Different concentrations of MNF and MNS dispersions (41.25, 82.5, 165, 330 μg mL^{-1}) were made up in water. Then 120 μL of Broth, 13 μL of bacteria (1.6×10^4 CFU) and 67 μL of each material were added to a 96-well plate.

The plate was incubated in a Clariostar Alphascreen-certified plate reader for 24 h at 37 °C. The plate reader read the OD_{600} value of each well at 24 min intervals. Before each reading, the plate was shaken at 300 rpm for 20 s. Control wells were included, replacing material with sterile water. This control showed that the incubation conditions did not inhibit bacterial growth. The OD_{600} values were normalised to account for the absorbance of the MNF and MNS in the bacterial dispersions. Inhibition assays were carried out with three biological replicates of three technical replicates. The percentage inhibition was determined using eqn (1).

$$\text{Bacterial inhibition (\%)} = ((OD_{control} - OD_{sample})/OD_{control}) \times 100 \quad (1)$$

To assess the bacterial growth kinetics, OD_{600} values were plotted against time over the 24 h incubation period. The area under the growth curve (AUC) was calculated for each biological replicate using the trapezoidal rule in Microsoft Excel. Lower AUC values indicate reduced cumulative bacterial growth over the incubation period.[21]

Statistical analysis was performed using Microsoft Excel. One-way ANOVA was used to determine the effect of material concentration on bacterial inhibition and AUC values. Two-tailed *t*-tests were used for pairwise comparisons between MNS and MNF at equivalent concentrations and, where appropriate, between treated samples and the untreated control. Statistical significance was defined as $p \geq 0.05$, $*p < 0.05$, $**p < 0.01$, and $***p < 0.001$.

Membrane integrity measurement

The integrity of MNS- and MNF-treated membranes was examined using a propidium iodide (PI) assay. The PI staining was performed according to the manufacturer's protocol with minor modifications.[22] *E. coli* MG1655 were grown to 1.6×10^8 CFU mL^{-1}. Then 0.5 mL of bacterial suspension was added to 0.5 mL MNS or MNF dispersions (41.25, 82.5, 165, 330 μg mL^{-1} final concentration). These were incubated for 4 h at 37 °C, shaking at 225 rpm. Bacterial cells were then washed with PBS to remove excess MNS and MNF. A 1 μL PI solution (1 mg mL^{-1}) was added to 1 mL of the bacterial suspension, and the mixture was incubated in the dark at room temperature for 15 min. The samples were then read using a Clariostar Alphascreen-certified plate reader with an excitation of 535 nm and emission at 617 nm. Untreated bacterial cells were used as a negative control, and cells treated with 70% ethanol for 15 min were used as a positive control.

Thiol oxidation and quantification

The thiol concentration in glutathione was determined using the Ellman's assay,[23] following a method used to measure ROS-independent oxidative stress in graphene-based materials.[24] MNS and MNF were dispersed in 50 mM bicarbonate buffer (pH 8.6) at a concentration of 660 μg mL^{-1}. 225 μL of each was added to 225 μL of reduced glutathione (GSH) solution (0.4 M final concentration in bicarbonate buffer) in a 2 mL Eppendorf tube. The tubes were placed in a shaker at 150 rpm for incubation times of 2, 4, and 6 h. After incubation, 785 μL of Tris–HCl (0.05 M) and 15 μL of DNTB (100 mM) were added. The tubes were centrifuged at 2000 rpm to remove MNF and MNS. The absorbance of each solution was then recorded at 412 nm. GSH solution without any added MNF/MNS was used as a negative control. GSH (0.4 mM) oxidised by H_2O_2 (1 mM) was used as a positive control. The loss of GSH was calculated using eqn (2). This was repeated to determine the effect of the concentration of the MNS and MNF dispersions (final concentrations of 330, 165, 82.5, and 41.24 μg mL^{-1} were employed).

$$\text{\% GSH loss} = ((\text{absorbance} - \text{ve control} - \text{absorbance sample})/\text{absorbance of} - \text{ve control}) \times 100 \quad (2)$$

Detection of superoxide radical anion ($O_2^{\bullet -}$). ROS generation was assessed using the NBT reduction assay, as previously described, to determine ROS generation by graphene oxide.[25] In short, the ROS generation was determined in extracts from bacterial cells (*E. coli* and *S. aureus*) grown in liquid cultures. A 0.1 mL of bacterial suspension (OD_{600} = 1.0) was incubated with 0.1 mL of MNF/MNS dispersion at 37 °C. Material concentration and incubation time were varied to determine the effect of each parameter on $O_2^{\bullet -}$ production. A volume of 0.5 mL NBT (1 mg mL^{-1}) was incubated for a further 30 min at 37 °C. A volume of 0.1 mL of HCl (0.1 M) was then added to each sample to stop the reduction of NBT. The samples were centrifuged at 3000 rpm for 10 min. The blue pellet was collected and dissolved in 0.6 mL of DMSO and 0.8 mL of Hanks' buffered

salt solution. The absorbance of each sample was measured at 560 nm. Concentrations were varied with the following final MNS and MNF concentrations (330, 165, 82.5 and 41.24 μg mL^{-1}). Incubation time was also varied between 2, 4 and 6 h to determine the impact of time on $O_2^{\bullet -}$ production.

Detection of hydroxy radical (OH•). A terephthalic acid assay has previously been used to determine OH• generation by MoS_2-based material,[26] and it was employed in this study. 0.5 mM of TA in PBS buffer was incubated with different concentrations of MNF and MNS, ranging from 41.25 to 330 μg mL^{-1} for 4 h. The time dependence of MNF OH• production was also determined by incubating 0.5 mM TA with 330 μg mL^{-1} for 2, 4, 6, 8 and 24 h. Incubation was carried out at 37 °C and 225 rpm. After incubation, the MNS and MNF were removed by centrifugation. They were then analysed using PL spectra, obtained with a Cary Eclipse fluorescence spectrometer. All measurements were carried out in triplicate.

Results and discussion

Characterisation of the MoS_2 structures MNS and MNF

The MNS and MNF were characterised using a combination of XRD, XPS, SEM, TEM, and UV-visible spectroscopy to provide information on the crystallinity, chemical composition, and morphology of both structures. The XRD patterns of MoS_2 following exfoliation (s-MNS), and secondly following exfoliation combined with refluxing (MNS), are shown in Fig. 1(a), and the corresponding pattern is shown for MNF in Fig. 1(b). Diffraction analysis was carried out using the diffraction angle 2θ in the range of 10–90°. The refluxed MNS exhibits more intense, sharper peaks, indicating higher crystallinity than s-MNS. The XRD peaks at 14.37°, 28.99°, 32.66°, 33.48°, 35.85°, 39.53°, 44.13°, 49.77°, 55.98°, 58.32°, 60.12°, 60.41° can be attributed to the characteristic crystallographic planes found in the hexagonal phase of MoS_2 namely (002), (004), (100), (101), (102), (103), (006), (105), (106), (110), (008), (112), respectively. The phases of both the s-MNS and MNS were identified as hexagonal structures with the *P*63/*mmc* space group.[27] In contrast, the MNF data show much broader, less-defined peaks, Fig. 1(b). This is caused by the amorphous arrangement of the material, scattering the X-rays in many different directions. In particular, the broad peak centred around 20–30° is consistent with amorphous or poorly crystalline molybdenum oxide, suggesting the presence of some molybdenum oxide phases in the MNF. Similar XRD patterns have been observed in other hydrothermally synthesised MNF reported for a number of applications.[28,29]

The UV-vis absorption plots shown in Fig. 1(c) compare the optical properties of the three MoS_2 structures, MNF, MNS, and s-MNS, over the wavelength range 200 to 800 nm. The samples were dispersed in an EtOH : H_2O solution (50 : 50, 1 mg mL^{-1}) for 30 min. In Fig. 1(c), both s-MNS and MNS show distinct absorbance bands at 620 and 682 nm. These absorbance bands are characteristic of 2D exfoliated MoS_2 nanosheets, corresponding to direct transitions between the valence and

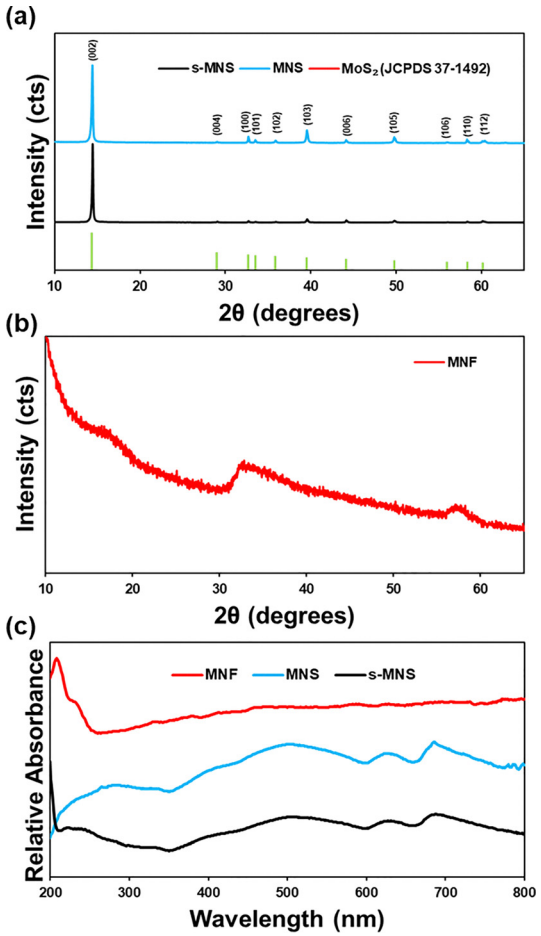

Fig. 1 XRD plots of (a) s-MNS (exfoliated MoS_2 sheets), MNS (refluxed following exfoliation) and JCP of MoS_2, (b) hydrothermally synthesised MoS_2 flowers and (c) UV-visible spectra for MNF, MNS and s-MNS.

conduction bands in the Brillouin zone.[30] Less distinct absorption bands are seen at 403 and 498 nm. These excitons arise from the direct electronic transitions near the *M* point of the Brillouin zone. These have been associated with smaller lateral-size nanosheets, due to their increased sensitivity to edge and confinement effects.[31] Interestingly, the MNS showed a ~90% increase in absorbance at these bands. This indicates a higher concentration of few-layered nanosheets compared to the s-MNS sample, which contains more bulk MoS_2. These absorption bands are largely absent in the UV-Vis spectra of MNF, indicating that this material lacks the 2D sheet-like nature of the MNS samples. For the most part, the spectrum of MNF is featureless. However, it has strong bands below 250 nm. Absorption in this region is characteristic of MoO_3.[32]

The XPS data were used to determine the oxidation state of the elements (Mo, S, O) present at the surface of both the MNS and MNF samples. Fig. 2 compares the Mo 3d, S 2p and O 1s XPS spectra of both samples. The MNS Mo 3d spectrum has two prominent peaks at 229.6 and 232.9 eV corresponding to Mo^{4+} $3d_{5/2}$ and $3d_{3/2}$, respectively. This spectrum also has two minor peaks at 233.8 and 236.7 eV corresponding to Mo^{6+} $3d_{5/2}$

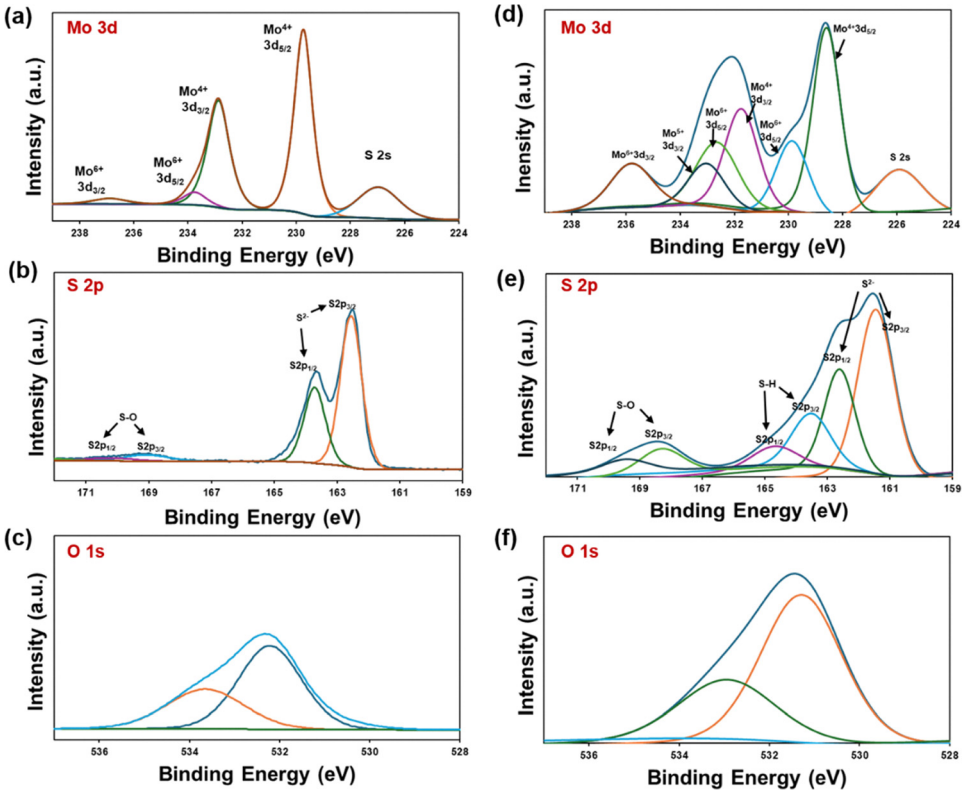

Fig. 2 XPS data recorded for MNS (a) Mo 3d, (b) S 2p, and (c) O 1s and MNF (d) Mo 3d, (e) S 2p and (f) O 1s.

and $3d_{3/2}$. These peaks arise from some partial oxidation of Mo in MoS_2. When comparing this spectrum to that of MNF, it includes two additional peaks corresponding to Mo^{5+} $3d_{5/2}$ and $3d_{3/2}$. There is a 0.9 to 1.1 eV shift of the Mo^{6+} and Mo^{4+} peaks to a lower binding energy caused by the presence of the intermediate Mo^{5+} state, leading to a change in the electron density around Mo. Similar shifts were seen in other MoO_3@MoS_2 heterostructures.[33] Both spectra also have a peak corresponding to S 2s at 227.1 and 225.9 eV, respectively, consistent with previous reports. The S 2p spectrum of MNS shows prominent peaks at 162.5 and 163.8 eV, corresponding to S^{2-} S $2p_{3/2}$ and S $2p_{1/2}$, respectively. These peaks confirm the presence of MoS_2. There are also two small peaks at 233.8 and 236.7 eV, corresponding to oxidised sulfur from air exposure. The S 2s spectra for the MNF sample show the prominent S^{2-} S $2p_{3/2}$ and S $2p_{1/2}$ peaks at 161.4 and 162.5 eV, showing that MoS_2 is also present in this sample. However, it has more prominent peaks corresponding to oxidised sulfur at 168.2 and 169.4 eV. These peaks indicate that some sulfur is present as SO_4^{2-}. There are also two peaks corresponding to sulfur in the form of thiols at 163.5 and 164.7 eV. These peaks can be attributed to thiol groups from the sulfur precursor used in the hydrothermal synthesis. When comparing the O 1s spectra of the MNS and MNF samples, they both have lattice oxygen peaks at 532.2 and 531.2 eV, respectively. The MNF peak has a significantly higher intensity than the MNS peak, indicating increased oxygen content at the MNF surface due to the formation of molybdenum oxide species.

The surface morphologies of MNS and MNF samples were examined using SEM and TEM, and these micrographs are shown in Fig. 3 and 4, respectively. The higher resolution SEM micrographs in Fig. 3(a) and (b) show the morphology of the MNS and MNF, respectively. The MNF structures appear as particles aggregated into feathery, hierarchical clusters resembling snowflakes or nanoflowers. These form three-dimensional architectures with high surface roughness, consistent with hydrothermal synthesis. On the other hand, the MNS show the presence of sheets, revealing flatter, thinner structures with sharply defined edges, typical of exfoliation processes. The lower-resolution images in Fig. 3(c) and (d) depict hydrothermally formed MoS_2 as a dense network of flower-like clusters with high interconnectivity, while the monolayer-like sheets are arranged in a more planar, partially restacked configuration, indicating successful exfoliation. The TEM images presented in Fig. 4 reveal clear differences in the morphology and crystallinity of MNS and MNF. As shown in Fig. 4(a), the MNF displays sponge-like crumpled networks. In Fig. 4(b), the edge-on view of the MNF is visible in the inset, while the selected-area electron diffraction (SAED) shows a diffuse, ring-like pattern rather than discrete Bragg spots. The absence of well-defined reflections suggests that the MNF has poor crystallinity or consists of small crystallites within the amorphous regions. In contrast, the TEM image of the MNS reveals sharp edges that are clearly shown in Fig. 4(c), while the higher resolution image depicted in Fig. 4(d) shows thin, transparent sheets with irregular, faceted edges and wrinkled

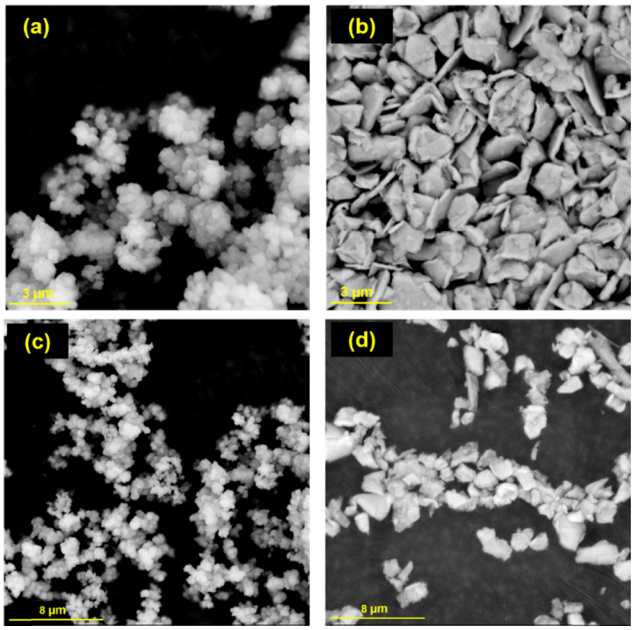

Fig. 3 SEM images (a) and (c) of MNF and (b) and (d) of MNS at different resolutions.

surfaces, consistent with few-layered MoS_2 nanosheets. The micrograph in Fig. 4(e) shows the MNS with a rippled appearance. The parallel fringes indicate high crystallinity, with regions of varying contrast suggesting a few-layer thickness of the MoS_2 sheets. The corresponding SAED pattern (Fig. 4(f)) indicates the characteristic hexagonal symmetry, confirming the crystalline nature of the MoS_2 nanosheets. Well-defined diffraction spots corresponding to the (100), (110), and higher-order planes of the hexagonal 2H MoS_2 phase are clear. This is indicative of a few-layer stacking without significant defects or phase impurities and is consistent with other reported MoS_2 nanosheets.[34]

To gain further insight into the nature of the MNS and MNF, dynamic light scattering and Zeta potential measurements were carried out, and the corresponding data are summarised in Fig. 5. In this study, four MNS families with sheets of different sizes were employed, as outlined in Table 1. Particle size analysis showed that the MNS size isolation successfully produced sheets of various sizes. This is illustrated in Fig. 5(a), where further centrifugation results in smaller MNS sheets. The MNF were found to have an average size of 691 nm, which compares well with the size of the MNS sheets following three to four centrifugation steps. As shown in Fig. 5(b), the MX MNS sample exhibited a much greater variation in size, which was expected because it included all sizes. In contrast, the polydispersity index improved as the sizes were isolated. The first isolate had the poorest polydispersity (0.357) with a large deviation (0.147). The polydispersity index decreases as the sheet size decreases, with isolate 4 having a narrow size distribution (PDI = 0.158). The MX MNS has the largest size distribution (PDI = 0.502). MNF showed a narrow size distribution (PDI = 0.236). The values for MNF and MNS (2, 3 and 4) fall within the range generally considered acceptable for nanoparticle suspensions (<0.3).[35] Typically, nanoflowers display slightly higher heterogeneity than nanosheets, consistent with their more complex morphology.[36] Zeta potential analysis was used to determine the surface charge of the nanostructures in dispersion. After the removal of the MNS isolate 1, the other MNS samples showed a zeta potential between −27.17 and

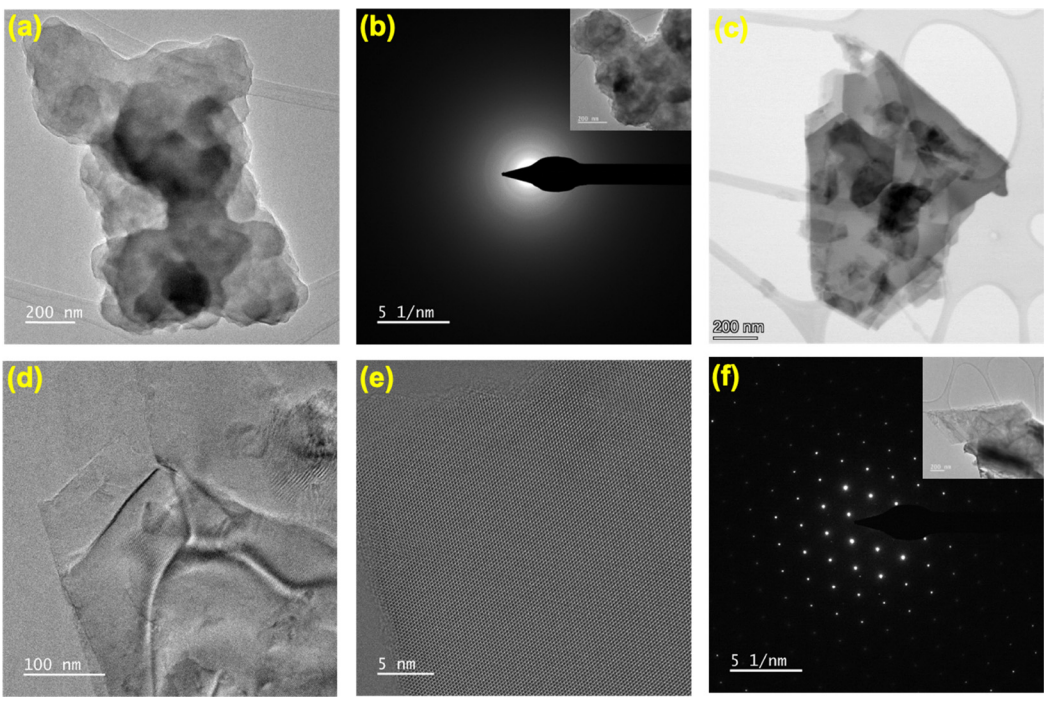

Fig. 4 TEM analysis of MNS and MNF (a) MNF image, (b) MNF SAED pattern, (c)–(e) MNS images at different resolutions, (f) MNS SAED pattern.

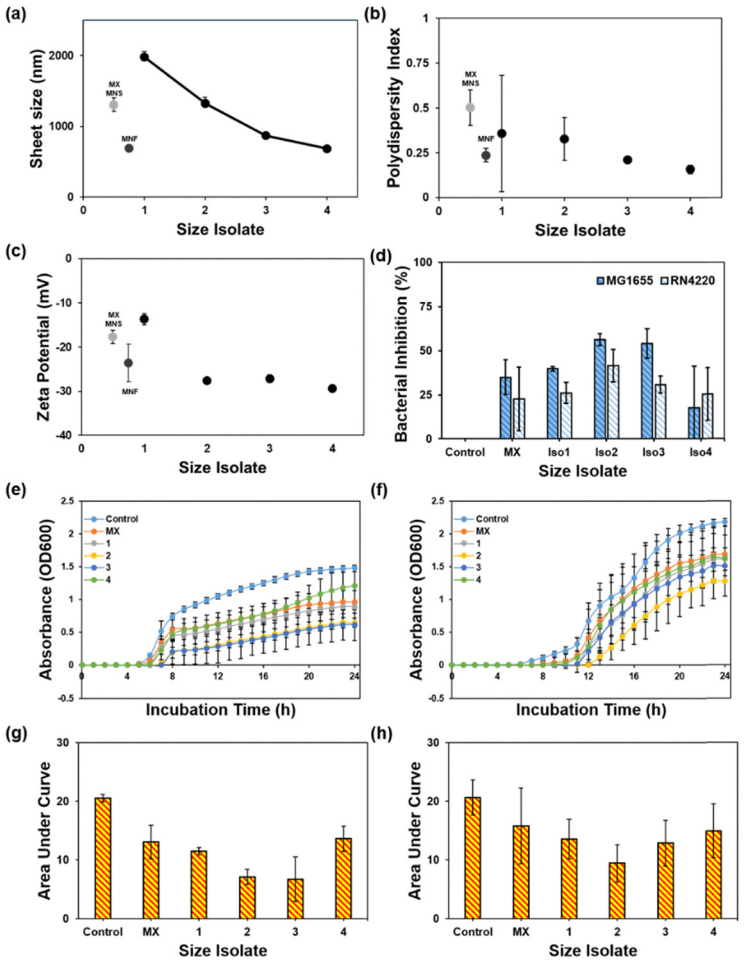

Fig. 5 (a) sheet size, (b) polydispersity, (c) zeta potential and (d) bacterial growth (e) bacterial growth kinetics of *E. coli* MG1655 (f) bacterial growth kinetics of *S. aureus* RN4220 (g) and (h) are under the growth curve (AUC) as a function of processing using centrifugation (Table 1).

Table 1 Size separation conditions employed for MNS, where MX refers to mixed sizes

Sample isolate	Centrifugation speed (rpm)	Centrifugation time (min)
MX	0	0
1	1000	10
2	2000	10
3	3000	10
4	4000	10

−29.38 mV. MNF demonstrated a zeta potential of −23.57 (RSD = 4.244). MNS indicates superior stability in dispersion, as zeta potentials in the vicinity of −30 mV are indicative of strong electrostatic repulsion.[37] The MX and 1st isolate exhibit a lower surface charge. This is consistent with previous studies where bulk MoS_2 has a less negative surface charge than few-layered, exfoliated sheets.[38] The lower zeta potential of MNF indicates a higher risk of nanoflower aggregation and reduced colloidal stability. These PDI and zeta potential values imply that MNS (second, third and fourth isolates) have better dispersibility in biological media. To determine whether nanosheet size influenced antibacterial activity, the mixed MNS sample (MX) and each size-isolated fraction were incubated with *E. coli* and *S. aureus* at 330 μg mL^{-1}. The resulting bacterial inhibition is shown in Fig. 5(d). Although isolate 2 exhibited the greatest mean inhibition against both bacterial strains, one-way ANOVA indicated that nanosheet size significantly influenced antibacterial activity only against *E. coli* (p = 0.018), whereas no significant effect was observed for *S. aureus* (p = 0.367). Planned pairwise comparisons between the mixed-size sample and each isolated fraction using two-tailed t-tests did not identify any statistically significant differences ($p > 0.05$). The average bacterial growth kinetics for the mixed-size sample and each isolated nanosheet fraction are shown in Fig. 5(e) and (f). Consistent with the endpoint inhibition measurements, Isolate 2 produced the greatest delay in bacterial growth for both *E. coli* and *S. aureus*, whereas the remaining isolates produced similar growth profiles. To quantify cumulative bacterial growth over the entire incubation period, the area under the growth curve (AUC) was calculated (Fig. 5(g) and (h)). AUC analysis showed a progressive reduction in cumulative bacterial growth for the isolated nanosheets relative to the

mixed sample, with isolate 2 exhibiting the lowest mean AUC for both bacterial species. However, pairwise comparisons between the mixed-size sample and each isolated fraction did not reveal statistically significant differences ($p > 0.05$), indicating that although size isolation altered the average antibacterial response, no individual isolate produced significantly greater cumulative growth inhibition than the mixed-size sample under the conditions investigated. As isolate 2 exhibited the highest mean antibacterial activity, it was selected for all subsequent experiments.

Antibacterial activity of MNS and MNF dispersions. As shown in Fig. 6, MNS exhibited concentration-dependent inhibition of both *E. coli* and *S. aureus*, whereas MNF exhibited strong inhibition of *S. aureus* but comparatively limited inhibition of *E. coli*. In Fig. 6(a), the inhibition of *E. coli* by both MNS and MNF is shown. MNS shows a concentration-dependent inhibition, inhibited by 50.79% after 24 h of incubation at 330 μg mL^{-1}. On the other hand, MNF shows a more limited inhibition of *E. coli* across all concentrations, with inhibition increasing from 5.55% to 22.08% as the MNF concentration

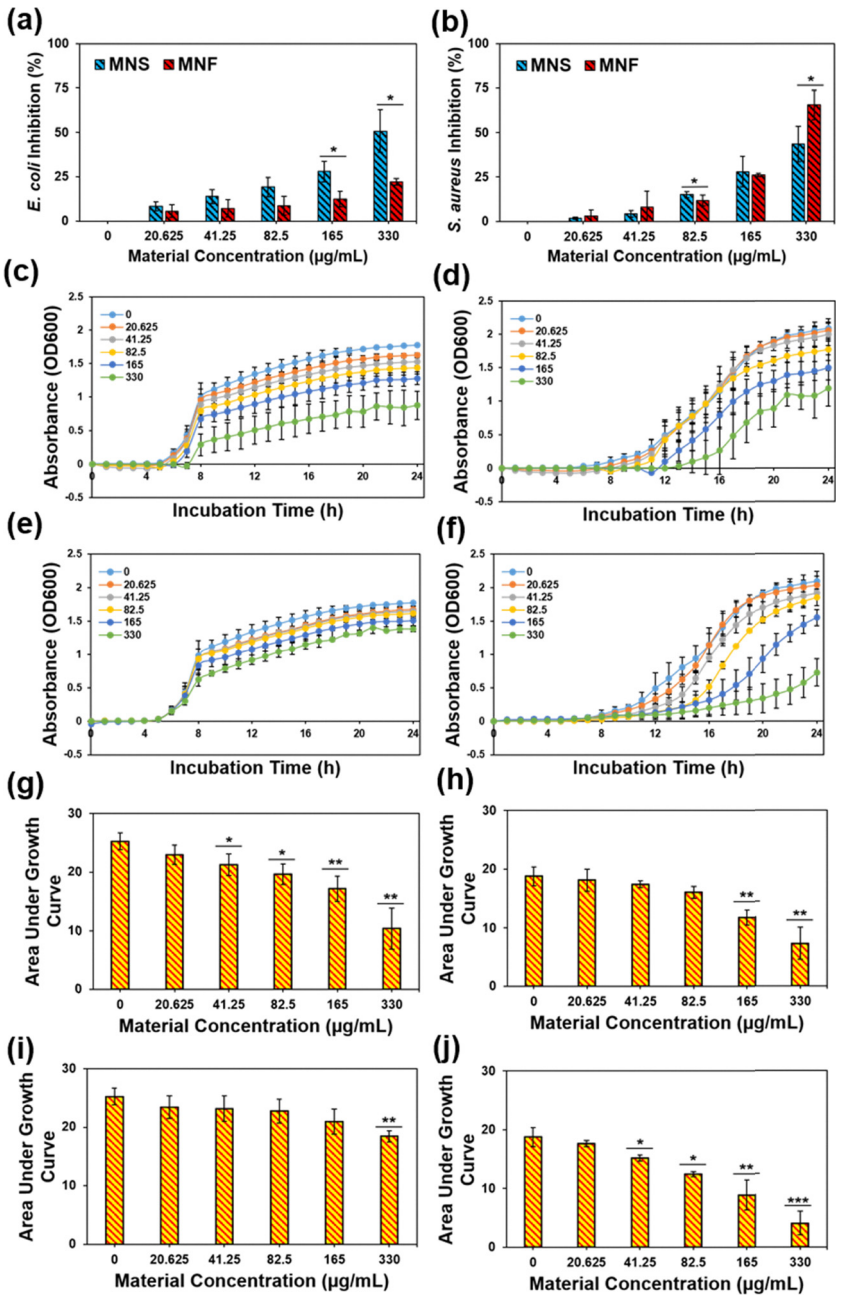

Fig. 6 Antibacterial activity of MNS and MNF against (a) *E. coli* and (b) *S. aureus* growth inhibition as a function of concentration of MNS and MNF following 24 h incubation. Growth kinetics of (c) *E. coli* treated with MNS, (d) *S. aureus* treated with MNS, (e) *E. coli* treated with MNF, and (f) *S. aureus* treated with MNF. Area under the bacterial growth curves (AUC) for (g) *E. coli* treated with MNS, (h) *S. aureus* treated with MNS, (i) *E. coli* treated with MNF, and (j) *S. aureus* treated with MNF. Data are presented as mean ± SD (n = 3).

increases from 20.62 to 330 μg mL^{-1}. In Fig. 6(b), the inhibition of *S. aureus* by both MNS and MNF is shown. As MNS concentration increases from 20.6 to 330 μg mL^{-1}, bacterial inhibition increases from 1.75 to 43.52%. Inhibition during incubation with MNF increases from 2.93 to 65.52%. One-way ANOVA demonstrated a significant effect of concentration on bacterial inhibition within each material. MNS showed statistically significant inhibition of both *E. coli* ($p < 0.0001$) and *S. aureus* ($p < 0.0001$). MNF showed statistically significant inhibition of *S. aureus* ($p < 0.0001$), but non-significant inhibition of *E. coli* ($p > 0.05$). Two-sample *t*-tests were performed to compare the antibacterial activity of MNS and MNF at each concentration. Significant differences were observed at 165 and 330 μg mL^{-1} against *E. coli* ($p < 0.05$) and at 82.5 and 330 μg mL^{-1} against *S. aureus* ($p < 0.05$).

The average bacterial growth kinetics of MNS- and MNF-treated cultures over 24 h are shown in Fig. 6(c–f). The absorbance at 600 nm (OD_{600}) is proportional to bacterial cell concentration over a limited linear range.[39] Fig. 6(c) shows that increasing concentrations of MNS prolong the lag phase of *E. coli*, with the highest concentrations delaying the onset of exponential growth relative to the untreated control. MNS similarly prolonged the lag phase of *S. aureus* as shown in Fig. 6(d). The addition of MNF at increasing concentrations successfully prolonged the lag phase of *S. aureus* (Fig. 6(f)). In contrast, increasing concentrations of MNF produced only a modest delay in *E. coli* growth (Fig. 6(e)), indicating a substantially weaker effect on early bacterial proliferation than that observed for MNS.

While the growth curves qualitatively demonstrate delayed bacterial proliferation, area under curve (AUC) analysis provides a quantitative measure of cumulative bacterial growth throughout the incubation period. Unlike endpoint inhibition measurements, AUC incorporates the entire bacterial growth profile, providing a quantitative assessment of both delayed growth and reduced final biomass. Lower AUC values indicate that bacterial growth was suppressed over the entire experiment rather than only at the endpoint. AUC was calculated to determine the cumulative effect of MNS and MNF on bacterial growth. The AUC analysis for the growth curves is shown in Fig. 6(g)–(j). Both MNS and MNF reduced the AUC relative to the untreated control, indicating suppression of cumulative bacterial growth throughout the incubation period. One-way ANOVA revealed a significant effect of concentration on the AUC within each material. MNS showed high significance with both *E. coli* ($p < 0.0001$) and *S. aureus* ($p < 0.0001$). MNF showed statistically significant AUC change of *S. aureus* ($p < 0.0001$), and a less significant change with *E. coli* ($p < 0.05$). Two-sample *t*-tests were performed to compare the AUC for each concentration of MNS and MNF to that of the untreated control. Pairwise comparisons demonstrated that reductions in AUC became progressively more significant as material concentration increased. These reductions in AUC are consistent with the observed growth kinetics, where increasing material concentrations prolonged the lag phase and reduced cumulative bacterial proliferation. Direct comparison of the AUC values for MNS and MNF demonstrated no significant difference against *E. coli* ($p > 0.05$), whereas significant differences were observed against *S. aureus* at 41.25 μg mL^{-1} ($p < 0.001$) and 82.5 μg mL^{-1} ($p < 0.05$). The concentration-dependent reduction in AUC closely reflected the inhibition data presented in Fig. 6(a) and (b), demonstrating that the increased endpoint inhibition resulted from sustained suppression of bacterial growth throughout the incubation period rather than only at the final time point.

Control experiments were carried out to account for any antimicrobial activity that could be caused by the presence of molybdate and thiol species in the MNF structure. Neither of these impurities showed any significant inhibition of *E. coli* or *S. aureus* after 24 h. With this control, it can be concluded that the difference in antimicrobial activity derives primarily from morphological differences rather than from the slight difference in chemical composition.

Antibacterial mechanism of MNS and MNF. To investigate how MNS and MNF inhibit bacterial growth, different oxidative stress-mediated mechanisms were explored. Oxidative stress can result from the generation of reactive oxygen species (ROS) by nanomaterials. ROS-independent oxidative stress can also occur, involving nanomaterials that disturb or oxidise vital cellular components without generating ROS.

Firstly, a PI assay was performed to detect any membrane damage caused by the MNS and MNF treatments, as PI can only penetrate bacterial cells with compromised membranes.[40] The fluorescent intensity (RFU) was measured for MNS- and MNF-treated cells along with untreated cells (negative control) and 70% ethanol treated cells (positive control).[41] There was no increase in RFU for MNS- or MNF treated cells (31.2 and 27.4 RFU, respectively) when compared to the negative control (46 RFU). The positive control (265.5 RFU) demonstrated increased fluorescence. These findings suggest that the treatment did not cause significant membrane damage in either bacterial strain. The TEM images (Fig. 4) show folding within the structure, implying pliability in MNS that is not seen in MNF. The high surface area of MNS produces significant van der Waals forces, which can overcome any weak electrostatic repulsion between bacterial cells (surface charge ~ -15.0 mV) ((*E. coli*) and -30.0 mV (*S. aureus*))[42] and MNS (surface charge ~ -28 mV). MNF will not have the same strength of van der Waals forces due to its lack of well-defined crystallographic basal planes. The lack of observed membrane damage, coupled with the more significant inhibition by the MNS, aligns well with the previously reported wrapping/trapping physical mechanism.[16]

Ellman's assay. Glutathione oxidation was used to investigate the potential for ROS-independent oxidative stress. An Ellman's assay was employed to quantify GSH oxidation. GSH is a tripeptide with thiol groups. These thiol groups can be oxidised to disulfide, converting glutathione to glutathione disulfide. GSH acts as an antioxidant in bacterial cells, safeguarding cellular components from oxidative stress-induced damage.[43] Both MNS and MNF were incubated with GSH, and an Ellman's assay was used to determine GSH oxidation. GSH incubated

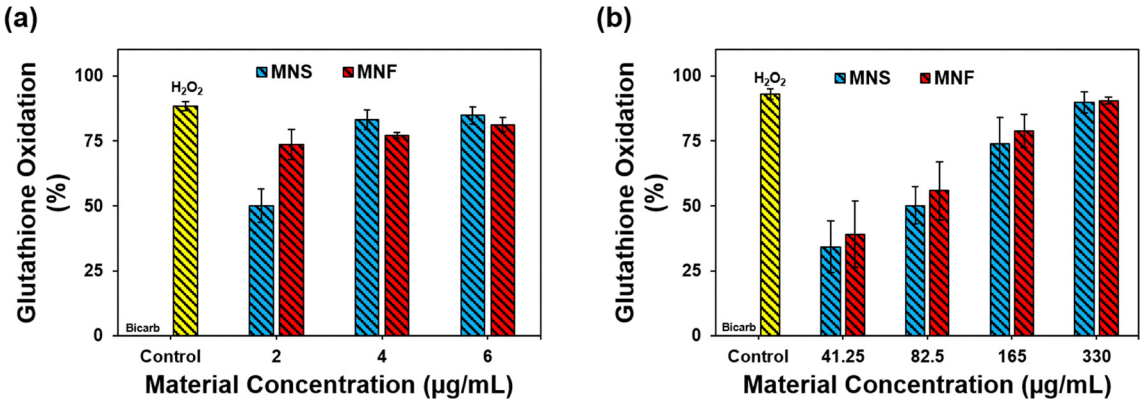

Fig. 7 GSH oxidation as a function of (a) incubation time for 330 μg mL^{-1} MNS and MNF and (b) concentrations of MNS and MNF following a 4 h incubation period.

with bicarbonate buffer (50 mM, pH 8.6) and H_2O_2 (1 mM) were used as a negative and positive control, respectively. The negative control demonstrated that incubation conditions and experimental method did not cause any GSH oxidation. Both MNS and MNF demonstrated a strong oxidation capacity that was dependent on both material concentration and incubation time, as illustrated in Fig. 7. MNF had a more immediate effect on GSH concentration. After 2 h incubation, MNF (330 μg mL^{-1}) had reduced GSH concentration by over 70%, whereas MNS (330 μg mL^{-1}) had only oxidised 50% of the GSH. Both MNF and MNS showed increased GSH oxidation as incubation time increased. After 6 h incubation, MNF and MNS oxidised 81.2% and 84.8%, respectively. Both MNS and MNF morphologies exhibited increasing oxidation capacity as concentration increased. MNF had a slightly stronger oxidation capacity at lower concentrations, with a 5% difference seen at 41.25, 82.5 and 165 μg mL^{-1}. However, at 330 μg mL^{-1}, both materials exhibited very similar oxidation capacities of approximately 90%. The time- and concentration-dependent nature of GSH oxidation is consistent with the antimicrobial activity of the MNS and MNF, as seen in Fig. 6. The strong ability of the MNS and MNF to oxidise glutathione illustrates their capacity to oxidise thiols and cellular components, which can cause bacterial death/inhibition.

Nitroblue tetrazolium assay. NBT is a commonly used assay to detect the presence of the superoxide radical ($O_2^{\bullet -}$).[44] Superoxide radicals are naturally produced by bacterial cells (*E. coli* and *S. aureus*) during their normal metabolic processes. However, when the concentration of these radicals accumulates beyond what the bacterial cells can manage due to oxidative stress, caused by external stressors, the excess ROS can damage cellular components such as lipids and proteins, causing cellular death.[45] An NBT assay was used to determine the ability of MNS and MNF samples to produce $O_2^{\bullet -}$. In the presence of $O_2^{\bullet -}$, the NBT in solution is reduced to form an NBT formazan, which is insoluble and can be collected as a blue precipitate. DMSO was then used to solubilise the formazan, and its absorption was measured at 560 nm. The ability of MNS and MNF to reduce NBT by producing $O_2^{\bullet -}$ was investigated by varying incubation time and material concentration. This superoxide measurement was performed by incubating both materials with *E. coli* and *S. aureus*. NBT was incubated with bacteria alone to determine how much of the superoxide detected was produced during natural cellular processes. Fig. 8(a) shows the effect of incubation time on $O_2^{\bullet -}$ production. After incubation for 2 and 4 h, MNF (330 μg mL^{-1}) showed a greater ability to produce superoxide. Superoxide concentration detected in both the MNS (330 μg mL^{-1}) and MNF samples decreased slightly from 4 to 6 h. This is likely due to the degradation of superoxide over time, by spontaneous dismutation or enzymatic breakdown caused by bacteria-produced superoxide dismutase (SOD). Both of these pathways have been shown to allow bacterial cells to control $O_2^{\bullet -}$ concentrations.[46] The superoxide concentration in both controls (*E. coli* and *S. aureus*) increased over time, and the differential (between the materials and the control) superoxide production was greatest at 2 or 4 h. Fig. 8(b) shows the effect of material concentration of $O_2^{\bullet -}$ produced. As seen with GSH oxidation, increased concentration led to increased $O_2^{\bullet -}$ production. MNS showed a much more significant concentration-dependent increase in $O_2^{\bullet -}$ production compared to that of MNF. Fig. 8(c) and (d) show the $O_2^{\bullet -}$ generation in the *S. aureus*. The same trends in incubation time and concentration increase are observed. The $O_2^{\bullet -}$ levels are significantly lower in the *S. aureus* bacterial model.

Terephthalic acid assay. Terephthalic acid is commonly used to effectively detect the hydroxyl radical. Terephthalic acid (TA) itself is non-fluorescent, but when it reacts with hydroxyl radicals ($OH^{\bullet}$), it forms 2-hydroxyterephthalic acid (TAOH), which is strongly fluorescent.[47] The presence of TAOH is indicated by its characteristic fluorescent peak at approximately 405 nm. This assay is reliable for the detection of $OH^{\bullet}$ as TAOH cannot be oxidised by other ROS, which could be generated by MNS and MNF. Fig. 9(a) shows that MNS did not generate $OH^{\bullet}$ radicals as the terephthalic acid remained unchanged, and fluorescence was not observed. However, MNF did generate $OH^{\bullet}$. The generation of $OH^{\bullet}$ by MNF is shown to be concentration dependent, as highlighted in Fig. 9(b). MNF

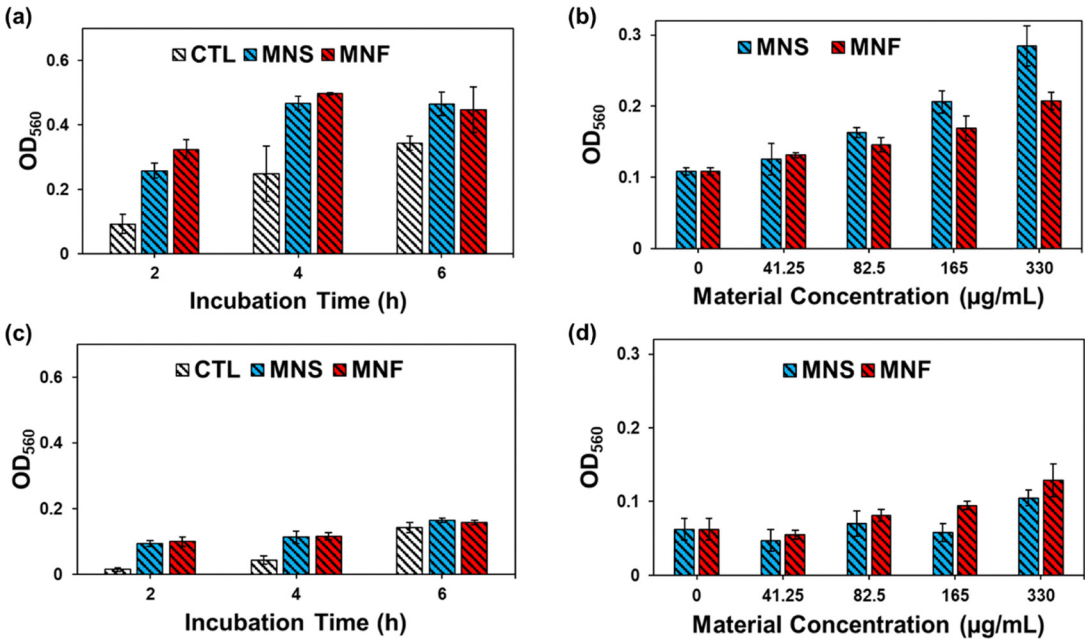

Fig. 8 NBT Formazan optical density measurements as a function of (a) incubation time for 330 μg mL^{-1} MNS and MNF with *E. coli*, (b) concentration of MNS and MNF with *E. coli* following 2 h incubation, (c) incubation time for 330 μg mL^{-1} MNS and MNF with *S. aureus* and (d) concentration of MNS and MNF with *S. aureus* following 2 h incubation.

demonstrated a rapid generation of $OH^{\bullet}$, with fluorescent intensity reaching 72.73 after 2 h. There was a small increase to 77.50 after 8 h, and 89.89 after 24 h (Fig. 9(c)). Similar $OH^{\bullet}$ generation has been observed in other defect-rich Mo-based nanostructures, such as Mo-QD.[26] MNF contains a combination of Mo oxidation states, making it a suitable candidate for $OH^{\bullet}$ generation. This combination has been shown to enable catalytic redox cycling,[48] which could catalyse the formation of $OH^{\bullet}$ from dissolved O_2.

A three-step antibacterial mechanism has been proposed for carbon-based nanomaterials, which consists of (i) direct contact with the bacteria and nanomaterial, (ii) an intimate membrane disruption and then (iii) further disruption of specific bacterial processes by oxidising cellular components.[24] It has been reported that bacterial inhibition by MoS_2 morphologies in the absence of light activation is more dependent on direct membrane interaction and GSH oxidation than on ROS-dependent oxidative stress.[49] The MNS

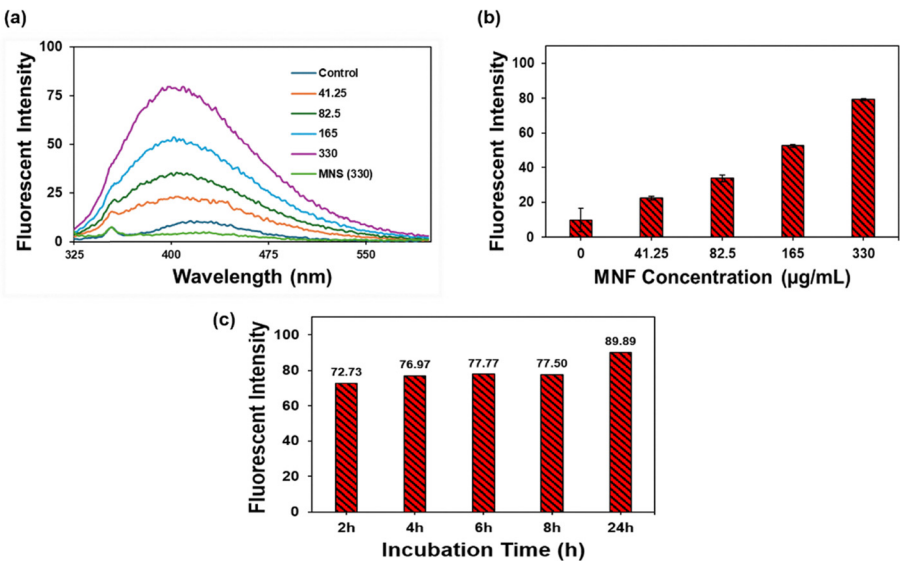

Fig. 9 TA assay results (a) Fluorescence spectra for the TA assay in the presence of concentrations of MNF and 330 μg mL^{-1} MNS with the excitation wavelength at 315 nm, and fluorescent intensity of the TA assay in the presence of MNF as a function of (b) the concentrations of MNF, and, (c) incubation time (330 μg mL^{-1} MNF).

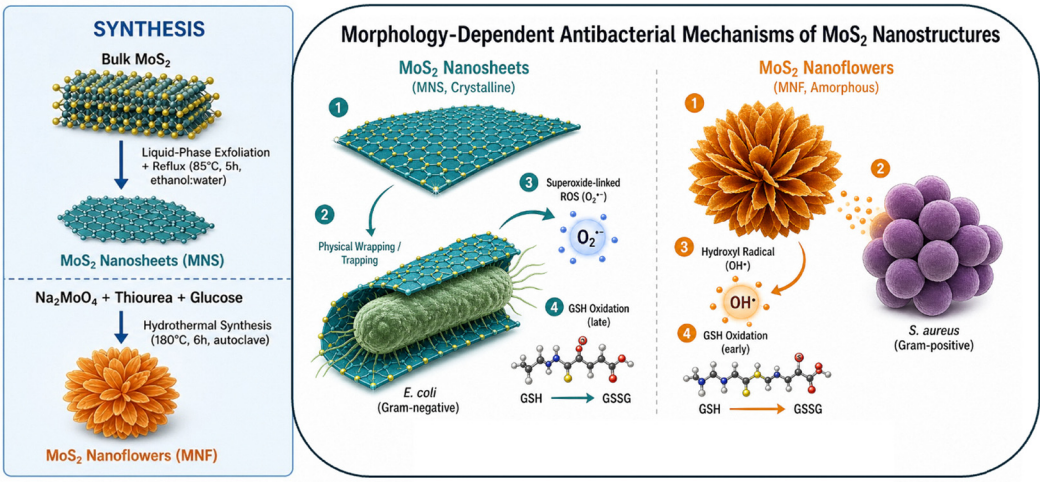

Scheme 1 Schematic representation of the MNS and MNF and their morphology-dependent antibacterial activities.

demonstrates a significant dependence on GSH oxidation, accompanied by some ROS generation, which supports a physical wrapping or trapping mechanism. The inhibition mechanism of MNF relies exclusively on oxidative stress, mediated by glutathione oxidation and the generation of multiple reactive oxygen species (ROS). This is illustrated more clearly in Scheme 1.

Conclusion

The comparative analysis of MNS and MNF reveals several distinct differences in the morphology, composition and antibacterial activity between the nanostructures. XRD and TEM analyses confirmed that MNS exhibit a crystalline structure, whereas MNF exhibit a largely amorphous structure. XPS revealed differences in chemical composition between MNS and MNF, highlighting slight oxidation in MNS and the presence of Mo^{5+} in MNF. SEM and TEM analysis confirmed the morphological differences between MNS and MNF. DLS and Zeta potential measurements demonstrated smaller size, greater uniformity, and greater dispersibility of MNS, highlighting their superior dispersibility.

Biological assays demonstrated that both MNS and MNF possess antibacterial activity against *E. coli* (Gram-negative) and *S. aureus* (Gram-positive), with efficacy dependent on both concentration and morphology. MNS exhibited greater antibacterial activity against *E. coli*, whereas MNF showed enhanced activity against *S. aureus*. Significant differences between the two morphologies were observed at selected concentrations, demonstrating that morphology influences antibacterial performance in a species-dependent manner. Growth kinetic analysis further demonstrated that increasing material concentration prolonged the bacterial lag phase and suppressed bacterial proliferation. This was supported by area under the growth curve (AUC) analysis, which confirmed that higher material concentrations reduced cumulative bacterial growth throughout the incubation period rather than only at the experimental endpoint.

Mechanistic investigations using Ellman's and NBT assays indicate that both nanostructures generate oxidative stress through ROS-dependent and ROS-independent pathways, with MNF producing more immediate effects and MNS displaying sustained oxidative capacity over time.

The findings in this study suggest that the antibacterial properties of MoS_2-based structures can be optimised by modifying morphology, crystallinity and chemical composition. Tuning these properties allows for targeted antibacterial applications. The performance difference between the prepared MNS and MNF illustrates the importance of nanostructure design in developing nanomaterial-based antimicrobials to combat antimicrobial resistance.

Author contributions

Joseph Monahan: investigation, methodology, formal analysis, data curation, validation, visualization, writing – original draft preparation, writing – review & editing; Shauna O'Shea-Boland: methodology, formal analysis, data curation, validation; Fiona Walsh: conceptualization, funding acquisition, resources, supervision, writing – review & editing; Carmel B. Breslin: conceptualisation, funding acquisition, project administration, resources, supervision, writing – review & editing, writing – original draft preparation.

Conflicts of interest

The authors have no conflicts of interest.

Data availability

Data will be made available on request.

Acknowledgements

BMG Clariostar multi-mode microplate reader is funded with the financial support of Research Ireland (SFI) under grant number 16/RI/3399. The authors would also like to acknowledge and thank Matthew Snelgrove, Temilade Esther Adegoke and Fathima Laffir in the Bernal Institute, University of Limerick, Ireland, for recording the XRD, TEM and XPS data. We acknowledge the Kathleen Lonsdale Human Health Institute, Maynooth University, for funding Joseph Monahan and Shauna O'Shea-Boland.

References

1 C. J. L. Murray, K. S. Ikuta, F. Sharara, L. Swetschinski, G. Robles Aguilar, A. Gray, C. Han, C. Bisignano, P. Rao, E. Wool, S. C. Johnson, A. J. Browne, M. G. Chipeta, F. Fell, S. Hackett, G. Haines-Woodhouse, B. H. Kashef Hamadani, E. A. P. Kumaran, B. McManigal, S. Achalapong, R. Agarwal, S. Akech, S. Albertson, J. Amuasi, J. Andrews, A. Aravkin, E. Ashley, F.-X. Babin, F. Bailey, S. Baker, B. Basnyat, A. Bekker, R. Bender, J. A. Berkley, A. Bethou, J. Bielicki, S. Boonkasidecha, J. Bukosia, C. Carvalheiro, C. Castañeda-Orjuela, V. Chansamouth, S. Chaurasia, S. Chiurchiù, F. Chowdhury, R. Clotaire Donatien, A. J. Cook, B. Cooper, T. R. Cressey, E. Criollo-Mora, M. Cunningham, S. Darboe, N. P. J. Day, M. De Luca, K. Dokova, A. Dramowski, S. J. Dunachie, T. Duong Bich, T. Eckmanns, D. Eibach, A. Emami, N. Feasey, N. Fisher-Pearson, K. Forrest, C. Garcia, D. Garrett, P. Gastmeier, A. Z. Giref, R. C. Greer, V. Gupta, S. Haller, A. Haselbeck, S. I. Hay, M. Holm, S. Hopkins, Y. Hsia, K. C. Iregbu, J. Jacobs, D. Jarovsky, F. Javanmardi, A. W. J. Jenney, M. Khorana, S. Khusuwan, N. Kissoon, E. Kobeissi, T. Kostyanev, F. Krapp, R. Krumkamp, A. Kumar, H. H. Kyu, C. Lim, K. Lim, D. Limmathurotsakul, M. J. Loftus, M. Lunn, J. Ma, A. Manoharan, F. Marks, J. May, M. Mayxay, N. Mturi, T. Munera-Huertas, P. Musicha, L. A. Musila, M. M. Mussi-Pinhata, R. N. Naidu, T. Nakamura, R. Nanavati, S. Nangia, P. Newton, C. Ngoun, A. Novotney, D. Nwakanma, C. W. Obiero, T. J. Ochoa, A. Olivas-Martinez, P. Olliaro, E. Ooko, E. Ortiz-Brizuela, P. Ounchanum, G. D. Pak, J. L. Paredes, A. Y. Peleg, C. Perrone, T. Phe, K. Phommasone, N. Plakkal, A. Ponce-de-Leon, M. Raad, T. Ramdin, S. Rattanavong, A. Riddell, T. Roberts, J. V. Robotham, A. Roca, V. D. Rosenthal, K. E. Rudd, N. Russell, H. S. Sader, W. Saengchan, J. Schnall, J. A. G. Scott, S. Seekaew, M. Sharland, M. Shivamallappa, J. Sifuentes-Osornio, A. J. Simpson, N. Steenkeste, A. J. Stewardson, T. Stoeva, N. Tasak, A. Thaiprakong, G. Thwaites, C. Tigoi, C. Turner, P. Turner, H. R. van Doorn, S. Velaphi, A. Vongpradith, M. Vongsouvath, H. Vu, T. Walsh, J. L. Walson, S. Waner, T. Wangrangsimakul, P. Wannapinij, T. Wozniak, T. E. M. W. Young Sharma, K. C. Yu, P. Zheng, B. Sartorius, A. D. Lopez, A. Stergachis, C. Moore, C. Dolecek and M. Naghavi, *Lancet*, 2022, **399**, 629–655.

2 C. A. Michael, D. Dominey-Howes and M. Labbate, *Front Public Health*, 2014, **2**, 145.

3 A. Kramer, I. Schwebke and G. Kampf, *BMC Infect. Dis.*, 2006, **6**, 130.

4 S. N. Redmond, B. S. Pearlmutter, Y. K. Ng-Wong, H. Alhmidi, J. L. Cadnum, S. Y. Silva, B. M. Wilson and C. J. Donskey, *Infect. Control Hosp. Epidemiol.*, 2021, **42**, 1076–1081.

5 Y. Wu, C. Li, H. C. van der Mei, H. J. Busscher and Y. Ren, *Antibiotics*, 2021, **10**, 623.

6 N. M. Dat, P. N. B. Long, D. C. U. Nhi, N. N. Minh, L. M. Duy, L. N. Quan, H. M. Nam, M. T. Phong and N. H. Hieu, *Synth. Met.*, 2020, **260**, 116260.

7 M. Li, Y. Liu, Y. Gong, X. Yan, L. Wang, W. Zheng, H. Ai and Y. Zhao, *Nanoscale Adv.*, 2023, **5**, 6278–6317.

8 M. Acerce, D. Voiry and M. Chhowalla, *Nat. Nanotechnol.*, 2015, **10**, 313–318.

9 W. Yin, J. Yu, F. Lv, L. Yan, L. R. Zheng, Z. Gu and Y. Zhao, *ACS Nano*, 2016, **10**, 11000–11011.

10 C. Zhang, D. F. Hu, J. W. Xu, M. Q. Ma, H. Xing, K. Yao, J. Ji and Z. K. Xu, *ACS Nano*, 2018, **12**, 12347–12356.

11 M. Salimi, M. A. Shokrgozar, D. H. Hamid and M. Vossoughi, *Mater. Res. Bull.*, 2022, **152**, 111837.

12 S. Cao, T. Liu, S. Hussain, W. Zeng, X. Peng and F. Pan, *Mater. Lett.*, 2014, **129**, 205–208.

13 H. Zhao, J. Zheng, W. Huang, Z. He, F. Huang, L. Zhang, T. Zhong, Y. Li, D. Xia, L. Shu and C. He, *J. Hazard. Mater.*, 2024, **480**, 136387.

14 X. Yang, J. Li, T. Liang, C. Ma, Y. Zhang, H. Chen, N. Hanagata, H. Su and M. Xu, *Nanoscale*, 2014, **6**, 10126–10133.

15 J. Kaur, M. Singh, C. Dell'Aversana, R. Benedetti, P. Giardina, M. Rossi, M. Valadan, A. Vergara, A. Cutarelli, A. M. I. Montone, L. Altucci, F. Corrado, A. Nebbioso and C. Altucci, *Sci. Rep.*, 2018, **8**, 16386.

16 M. Kumari and H. K. Kashyap, *Langmuir*, 2023, **39**, 5440–5453.

17 O. Akhavan, E. Ghaderi and A. Esfandiar, *J. Phys. Chem. B*, 2011, **115**, 6279–6288.

18 Q. Xu, P. Zhu, J. Zhang, Y. Liu, L. Cai, H. Jiang, M. Ji and J. Chen, *Mater. Lett.*, 2020, **271**, 127809.

19 D. Park, N. K. Kim, W.-R. Shin and C. O. Osuji, *ACS Appl. Mater. Interfaces*, 2025, **17**, 342–350.

20 J. Wu, T. Zhang, J. Qu, F. Z. Jiao, C. Hu, H. Y. Zhao, X. Li and Z. Z. Yu, *ACS Appl. Mater. Interfaces*, 2023, **15**, 29457–29467.

21 P. D. Tonner, C. L. Darnell, B. E. Engelhardt and A. K. Schmid, *Genome Res.*, 2017, **27**, 320–333.

22 Sigma-Aldrich, Bacteria Stain Propidium Iodide Solution (Product No. 79214): Data Sheet, Merck KGaA, Darmstadt, Germany, 2025, https://www.sigmaaldrich.com/deepweb/assets/sigmaaldrich/product/documents/175/383/79214dat.pdf?srsltid=AfmBOor3eqa2UlZgYuViItpRyVZhQp3JN7QnoE2KXpP6IuSGaIaRpYk.

23 G. L. Ellman, *Arch. Biochem. Biophys.*, 1959, **82**, 70–77.

24 S. Liu, T. H. Zeng, M. Hofmann, E. Burcombe, J. Wei, R. Jiang, J. Kong and Y. Chen, *ACS Nano*, 2011, **5**, 6971–6980.

25 S. Gurunathan, J. W. Han, A. Abdal Dayem, V. Eppakayala and J. H. Kim, *Int. J. Nanomed.*, 2012, **7**, 5901–5914.
26 S. R. Ali and M. De, *ACS Appl. Nano Mater.*, 2023, **6**, 2193–2202.
27 B. Schonfeld, J. J. Huang and S. C. Moss, *Acta Crystallogr., Sect. B*, 1983, **39**, 404–407.
28 X. Yang, L. Wen, H. Huang, Y. Wang, L. Wei and J. Yang, *Solid State Sci.*, 2022, **133**, 107014.
29 D. Wang, Z. Pan, Z. Wu, Z. Wang and Z. Liu, *J. Power Sources*, 2014, **264**, 229–234.
30 J. Zhang, H. Ouyang, X. Zheng, J. You, R. Chen, T. Zhou, Y. Sui, Y. Liu, X. A. Cheng and T. Jiang, *Opt. Lett*, 2018, **43**, 243–246.
31 P. Ni, M. Dieng, J.-C. Vanel, I. Florea, F. Z. Bouanis and A. Yassar, *Nanomaterials*, 2023, **13**, 2502.
32 A. V. Juan-Arturo, A. Leonel Mendoza-Martínez, G. Morales-Luna and M. Morales-Luna, *Adv. Phy.: X*, 2025, **10**, 2451687.
33 M. Faizan, S. Hussain, M. Islam, J.-Y. Kim, D. Han, J.-H. Bae, D. Vikraman, B. Ali, S. Abbas, H.-S. Kim, A. N. Singh, J. Jung and K.-W. Nam, *Nanomaterials*, 2022, **12**, 2008.
34 Q. D. Truong, M. Kempaiah Devaraju, Y. Nakayasu, N. Tamura, Y. Sasaki, T. Tomai and I. Honma, *ACS Omega*, 2017, **2**, 2360–2367.
35 A. M. Nasr, F. Moftah, M. A. S. Abourehab and S. Gad, *Pharmaceutics*, 2022, **14**, 2268.
36 S. J. Lee, H. Jang and D. N. Lee, *Nanoscale Adv.*, 2023, **5**, 5165–5213.
37 D.-D. Varsou, A. Afantitis, A. Tsoumanis, A. Papadiamantis, E. Valsami-Jones, I. Lynch and G. Melagraki, *Small*, 2020, **16**, 1906588.
38 M. Bae, J. K. Oh, S. Liu, N. Nagabandi, Y. Yegin, W. DeFlorio, L. Cisneros-Zevallos and E. M. A. Scholar, *Nanomaterials*, 2021, **11**, 1453.
39 K. Stevenson, A. F. McVey, I. B. N. Clark, P. S. Swain and T. Pilizota, *Sci. Rep.*, 2016, **6**, 38828.
40 M. Rosenberg, N. F. Azevedo and A. Ivask, *Sci. Rep.*, 2019, **9**, 6483.
41 B. Asadishad, S. Ghoshal and N. Tufenkji, *Environ. Sci. Technol.*, 2011, **45**, 8345–8351.
42 J. Monte, A. C. Abreu, A. Borges, L. C. Simões and M. Simões, *Pathogens*, 2014, **3**, 473–498.
43 H. J. Forman, H. Zhang and A. Rinna, *Mol. Aspects Med.*, 2009, **30**, 1–12.
44 J. Yang, Y. Cao and N. Zhang, *Spectrochim. Acta, Part A*, 2020, **239**, 118556.
45 S. Korshunov and J. A. Imlay, *J. Bacteriol.*, 2006, **188**, 6326–6334.
46 J. Fujii, T. Homma and T. Osaki, *Antioxidants*, 2022, **11**, 501.
47 L. Linxiang, Y. Abe, Y. Nagasawa, R. Kudo, N. Usui, K. Imai, T. Mashino, M. Mochizuki and N. Miyata, *Biomed. Chromatogr.*, 2004, **18**, 470–474.
48 Q. Yang, X. Gao, F. Song, X. Wang, T. Zhang, P. Xiong, Y. Bai, X. Liu, X. Liu, J. Zhang, G. Fu, Y. Tan, Y. Han and Q. Zhang, *JACS Au*, 2023, **3**, 3141–3154.
49 L. Mei, S. Zhu, W. Yin, C. Chen, G. Nie, Z. Gu and Y. Zhao, *Theranostics*, 2020, **10**, 757–781.

